Cephalopod-inspired snapshot multispectral sensor based on geometric phase lens and stacked organic photodetectors

Ali Altaqui[®],* Harry Schrickx, Sydney Gyurek, Pratik Sen[®], Michael Escuti, Brendan T. O'Connor, and Michael Kudenov

North Carolina State University, Department of Electrical and Computer Engineering, Raleigh, North Carolina, United States

Abstract. Multispectral imaging (MSI) is a valuable sensing modality for applications that require detecting a scene's chemical characteristics. Existing MSI techniques utilize a filter wheel or color filter arrays, which are subject to reduced temporal or spatial resolution. In this work, we present a cephalopod-inspired multispectral organic sensor (CiMOS) based on geometric phase lenses (GPLs) and organic photovoltaics (OPVs) to enable aberration-based color sensing. We mimic the approach by which animals with single-type photoreceptors perceive colors via chromatic aberration. The intrinsic chromatic aberration of GPLs allows for multispectral sensing by stacking precisely patterned OPVs within specific spectrally dependent focal lengths. We provide simulations and a proof of concept of the CiMOS and highlight its advantages, including its simple design and snapshot multi-color detection using only a single axial position. Experimental results demonstrate the sensor's ability to detect four colors with full width at half maximum spectral resolution as low as 35 nm. © 2022 Society of Photo-Optical Instrumentation Engineers (SPIE) [DOI: 10.1117/1.OE.61.7.077104]

Keywords: multispectral sensing; pancharatnam-berry phase; organic photovoltaics; geometric phase lens; imaging; sensors; spectroscopy.

Paper 20211173 received Oct. 13, 2021; accepted for publication Jun. 22, 2022; published online Jul. 21, 2022.

1 Introduction

Multispectral imaging (MSI) is an optical sensing method in which the spatial information of a scene is obtained across multiple spectral bands, forming a three-dimensional (3D) spatio-spectral data cube with dimensions (x, y, λ) . This technique is highly beneficial as it provides distinctive information about a scene, such as detecting the chemical features of materials. Some applications that use MSI include medicine, environment monitoring, geography, defense, and agriculture.

Conventional MSI techniques utilize prismatic or diffractive elements to disperse the light together with spatial scanning methods (e.g., whiskbroom⁷ or pushbroom⁸ scanners). Alternatively, color filter wheels can acquire the spectral dimension time-sequentially. Both spatial and spectral scanning methods are prone to temporal sampling artifacts and may require complex optomechanical elements. Existing snapshot MSI architectures overcome these limitations; however, they may necessitate complex or bulky designs, require a larger array size to capture the higher-order diffraction images, or add computational complexity to reconstruct the images. Novel detector designs, inspired by the eye of mantis shrimp, have also been reported to address some of the limitations of these prior architectures. 11–16

While the mantis shrimp's eye has driven extensive literature to present viable MSI detector designs, there have been other animals in nature capable of multispectral sensing via a vastly different optical detection mechanism. ^{17–19} Species of cephalopods are one good example. Squid, octopus, and cuttlefish have long been thought to be colorblind animals due to their possession of a single photoreceptor type, despite their ability to change skin color based on their

0091-3286/2022/\$28.00 © 2022 SPIE

^{*}Address all correspondence to Ali Altaqui, aaaltaqu@ncsu.edu

surroundings.²⁰ However, in recent research, Stubbs proposed a mechanism by which these animals achieve color discrimination by exploiting a combination of longitudinal chromatic aberration (CA), lens-to-retina displacement, and an off-axis pupil.²¹ Additionally, an MSI detector design inspired by octopus has been reported previously.^{22,23} It utilized spherical lenses to image a scene on a single focal plane (FP). This formed a chromatically aberrated image consisting of multiple spectral images with varying point spread functions (PSFs). A deconvolution algorithm was then applied to remove the chromatic aberrations and restore the spectral images. This technique suffers from various limitations, including its susceptibility to spectral crosstalk and spatial artifacts arising from the deconvolution algorithm and its requirement for distortion- and aberration-free optics to reconstruct the images with high accuracy (hence the need for multiple lenses).

In this paper, we report a new snapshot cephalopod-inspired multispectral organic sensor (CiMOS) structure based on a geometric phase lens (GPL) together with stacked organic photovoltaic (OPV) cells. Unlike the work by Zhan et al.,²² which collects blurred images at a single FP, the CiMOS device simultaneously collects multiple spectral channels at their sharpest focus by leveraging the CA of a single GPL. This is realized by cascading *N* OPVs along the same optical axis of the GPL, where *N* is the number of OPV layers. Each OPV is located at a specific detection plane away from the GPL, corresponding to the focal length of a nominal center (in- band) wavelength. The current embodiment incorporates four OPVs located at the focal length of 450-, 500-, 550-, and 650-nm wavelengths. Although the detectors in the current CiMOS structure and Ref. 12 are both classified as OPVs, there are differences in the materials selection and their physical and optical properties, including the responsivity and quantum efficiency. The OPVs in Ref. 12 were made polarization-sensitive to enable color filtering based on chromatic polarization interference. Conversely, the OPVs in the CiMOS design were isotropic, and their active area pitch was optimized to enable aberrated-based color filtering.

The CiMOS structure offers many advantages (derived from both the GPL and OPV elements) that collectively make it a simple, compact, and efficient snapshot MSI device. First, compared with a traditional refractive lens, the GPL is more than 10-fold thinner and features a flat surface on either side, enabling compact systems and flexible fabrication process. Additionally, as GPL is a unique type of diffractive element, it inherently manifests strong CA while offering near-unity diffraction efficiency. Although this is normally detrimental for most imaging systems, it is highly desirable in the CiMOS design. Moreover, with proper design of the geometric phase, GPL can be made aberration-free, surpassing the performance of traditional refractive lenses that exhibit multiple aberration components. While GPLs inherently function on polarized light, their diffraction efficiency and leakages can be made substantially more favorable than traditional diffractive lenses based on surface relief gratings, volume Bragg grating, or Fresnel surfaces and can therefore lead to higher contrast, wider field of view, broader spectral bandwidth, and more compact systems. Although the GPLs and GPL and GPLs are supported bandwidth, and more compact systems.

In addition to the GPL element, the OPV detectors also feature unique advantages including versatile processing on varied substrates and tuned spectral sensitivity.²⁸ The cells can be processed on transparent substrates using a variety of semitransparent electrodes and can be patterned simply through an array of additive and subtractive methods.²⁹ The versatility in the processing of these detectors allows for unique patterns, which enable spatially selective detection and transmittance of incident light. This makes organics attractive for focal volume array detection schemes and suitable for light-field or plenoptic imaging.³⁰ In our case, we leverage these features to fabricate small area detectors on glass substrates enabling snapshot spectral imaging through a tandem detector architecture. Meanwhile, the ability of these OPVs to be sensitive to a broad light spectrum is needed to enable multispectral detection.

It should be noted that prior MSI approaches exploiting the diffractive property of a chiral metalens have been reported.^{31–33} However, they require adjusting the camera's FP to detect multiple color images time sequentially. By comparison, our approach leverages the tandem OPV structure to enable snapshot multispectral detection.

Here, we show through simulations how the CiMOS structure leverages the synergy of GPL and OPVs to provide efficient snapshot multispectral sensing in a simple and compact detector architecture. A proof of concept is also experimentally demonstrated, and experimental results showcasing the spectral response of a single-pixel CiMOS detector are provided. While only a

single-pixel CiMOS design is demonstrated in this work, a two-dimensional (2D) image sensor can be realized through the use of geometric phase microlens array (GPLMA), which has been utilized previously to construct a snapshot imaging spectrometer.³⁴

2 Cephalopod's Light Sensing Mechanism

Figure 1(a) shows the eye of cuttlefish, a species that belongs to the class Cephalopoda. Generally, cephalopods possess unique off-axis pupil shapes ^{36–38} (a W-, U-, or dumbbell-shape), which enable light to enter their eye through the lens from many different directions, thereby accentuating CA. Figure 1(b) shows how CA is achieved in cephalopods. Light entering the pupil passes through the lens, which has a spectrally dependent index of refraction that is greater than the water's refractive index. Therefore, shorter wavelengths bends closer to the surface normal and longer wavelengths bend further resulting in different optical paths within the lens (with different spectral velocities). Upon exiting the lens, light's wavelengths refract away from the surface normal and toward the optical axis, resulting in different wavelengths optimally focused at different FPs. A larger off-axis pupil size (common to cephalopods) further maximizes the chromatic blurring due to off-axis rays traversing longer optical paths within the lens, yielding a greater angle of deviation. Only one wavelength will strike the photoreceptor cells at the optimal focus. Cephalopods possess a single photoreceptor type, so they require an additional mechanism in their eye to achieve color discrimination. This mechanism is best explained in Figs. 1(c)-1(e). Cephalopods have the ability to vary their accommodation range (defined as the lens displacement away from the retina) by means of changing the depth of their eyeball.²¹ They optimally focus longer/shorter wavelengths at the retina by moving their lens away from/ closer to the retina. The best accommodation is determined by a contrast method, i.e., mapping the scene's contrast to their focal settings, similar to how digital cameras obtain the best focus by maximizing contrast versus focal length. This requires a scene that has substantial spatial/spectral contrast so that variations in chromatic blurring can be detected.

Inspired by the cephalopod's eye, we also present a structure that leverages CA to discriminate various spectra. While cephalopods temporally scan their eyeball to determine the best

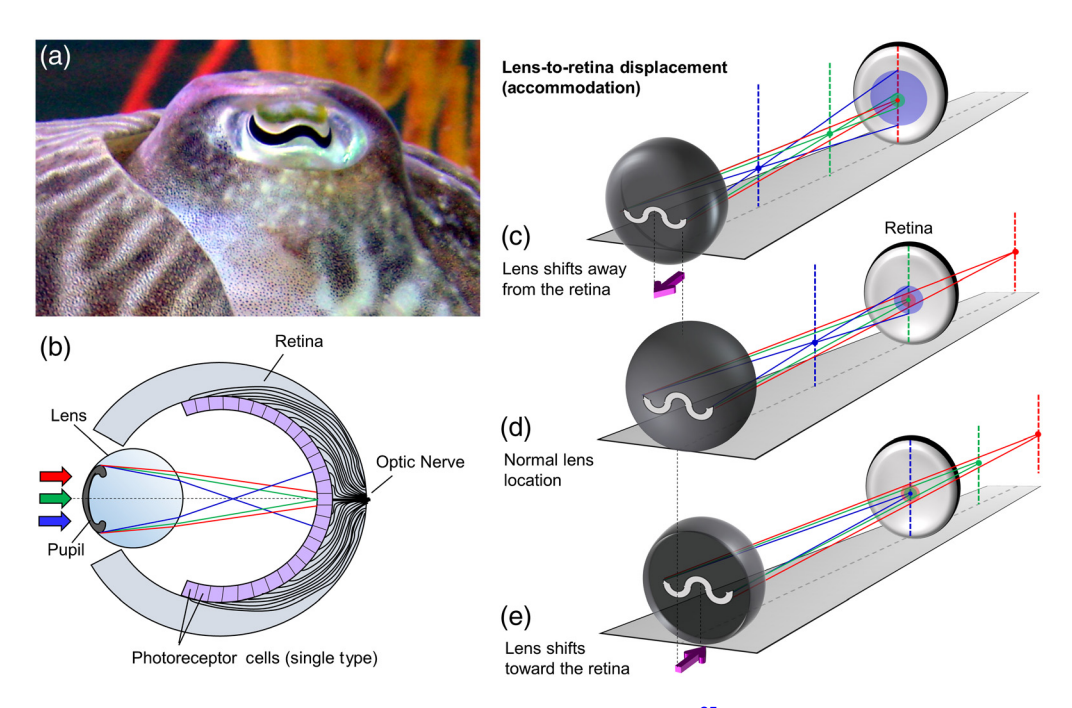


Fig. 1 Cephalopod's sensing mechanism. (a) Cuttlefish eye; (b) cross-section of the eye; (c)–(e) different accommodations; (c) lens shift away from the retina to focus the red light; (d) normal lens location; and (e) lens shift toward the retina to optimally focus blue light.

spectral focus at the optimal contrast, our CiMOS structure obtains the best focus for each wavelength simultaneously, without the need to move or scan any element in the system.

3 Geometric Phase Lens

The GPL is a unique type of diffractive lens that operates based on a geometric phase hologram. Unlike traditional refractive lenses, which need to be thick with curved surfaces to attain the desired bending power, GPLs do not depend on the refraction of light and, therefore, can be made thin and flat. Additionally, compared with traditional diffractive lenses (such as Fresnel lenses), GPLs only diffract the 0- and ± 1 -orders of light, thereby, maximizing the diffraction efficiency. Most importantly, GPLs induce a phase shift (Φ) on a traversing electromagnetic (EM) wave, known as the Pancharatnam–Berry phase, which largely depends on the optic axis' geometric distribution of an anisotropic material. This is achieved when an EM wave undergoes a continuous sequence of polarization transformation tracing a closed path in the Poincaré sphere. Although GPLs could incur color-dependent spherical aberration, this effect can be substantially mitigated with the appropriate design of the GPL phase profile as previously demonstrated in a GPL doublet or triplet lens system.

Figure 2 shows the GPL's concept. When an input light with arbitrary polarization states is incident on the GPL's surface, GPL produces three waves: a primary wave that converges at focal length +f, a conjugate wave that diverges with a focal length -f, and a leakage wave that maintains the path of the input light. The primary and conjugate waves are circularly polarized and mutually orthogonal, whereas the leakage wave retains the input wave's polarization states. For a plane-wave with random polarization $|\mathbf{E_{in}}\rangle$, defined by the Jones vector's ket notation, the output wave from the GPL is expressed as

$$|\mathbf{E}_{\mathbf{out}}\rangle = \sqrt{\eta_0}|\mathbf{E}_{\mathbf{in}}\rangle + \sqrt{\eta_{-1}}|\mathbf{R}\rangle e^{-j\Phi} + \sqrt{\eta_{+1}}|\mathbf{L}\rangle e^{j\Phi},\tag{1}$$

where $|\mathbf{R}\rangle$ and $|\mathbf{L}\rangle$ are the Jones vectors for right-hand circular polarized (RHCP) and left-hand circular polarized (LHCP) lights, respectively' η_0 , η_{+1} , and η_{-1} are the diffraction efficiencies for the 0-, +1-, and -1-order modes, respectively; $\Phi = 2\phi(r)$ is the geometric phase profile; and $\phi(r)$ is the local optic axis orientation (azimuth) of the anisotropic material as a function of the radial distance r from the center of the GPL.

Commonly, a GPL is fabricated as a half-wave (HW) retarder that has its optics axis in the plane of the film with ϕ spatially varied along r to form concentric rings of constant phase. Assuming an on-axis wave entering the GPL, the diffraction efficiencies are given as

$$\eta_0 = \cos^2\left(\frac{\delta}{2}\right),\tag{2}$$

$$\eta_{\pm 1} = \frac{1 \mp S_3'}{2} \sin^2\left(\frac{\delta}{2}\right),\tag{3}$$

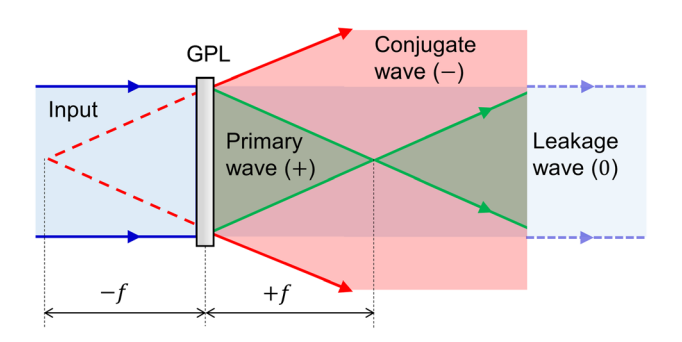


Fig. 2 The GPL's principle of operation.

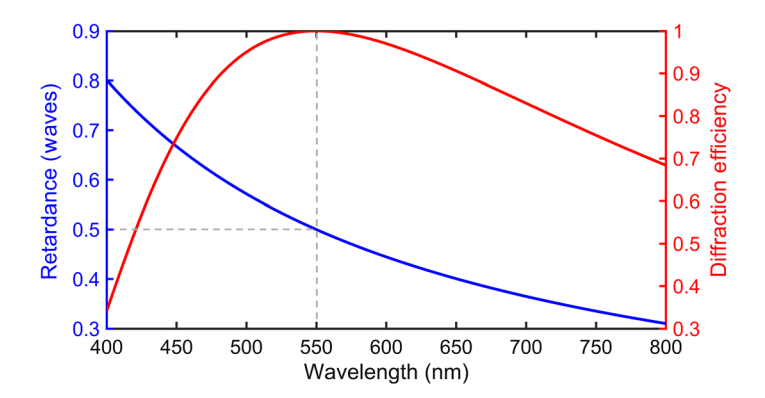


Fig. 3 Typical retardance and diffraction efficiency property of LCP-based GPL.

$$\delta(\lambda) = \frac{2\pi}{\lambda} \Delta n(\lambda) L,\tag{4}$$

where $\delta(\lambda)$ is the retardance as a function of wavelength; $S_3' = S_3/S_0$ is the normalized circular Stokes parameter of the incident light; S_0 is the total light's intensity; and $\Delta n(\lambda)$ and L are the birefringence and thickness of the film, respectively.

The diffraction efficiency of the primary wave η_{+1} depends on the input polarization and the retardance. Assuming that the GPL's material is made from the achromatic HW plate $(\delta = 180 \text{ deg for all } \lambda)$ and the input light is unpolarized or linearly polarized lights $(S_3' = 0)$, the diffraction efficiency η_{+1} drops by a factor of 2. If, however, the input light is LCHP $(S_3' = -1)$, η_{+1} is unity. For a wavelength-dependent HW retarder, η_{+1} is maximum at the design center wavelength.

We modeled the diffraction efficiency η_{+1} of a GPL that is similar to the one that we employed in our experiments. The GPL is designed for a 550-nm center wavelength and made from liquid crystal polymer (LCP) with $\Delta n(\lambda) = 0.12 + 8.3 \times 10^{-15} \,\lambda^{-2}$ and $L = 1.87 \,\mu\text{m}$. We also assumed the input light incident on-axis on the GPL with a perfectly LHCP state. Figure 3 shows the performance of the GPL's first order diffraction efficiency as a function of wavelength. At the GPL's design wavelength of 550 nm, the diffraction efficiency is 100%, with values ranging from 0.75 to 1 from 450 to 650 nm.

4 CiMOS Device – Theoretical System Model

The CiMOS structure is shown in Fig. 4. A collimated broadband light passes through a linear polarizer (LP) oriented at 0 deg with respect to the *x* axis, followed by an achromatic quarter waveplate (AQWP) with fast axis oriented at 45 deg with respect to the *x* axis. The output from the AQWP is a circularly polarized light. As a sign convention, we assume the light is RHCP from the point of view of the source. The RHCP light then passes a GPL made from LCP with a dispersion characteristic similar to the one simulated in Fig. 3. The GPL is oriented with the LCP surface facing the light source, causing an LHCP light to converge.

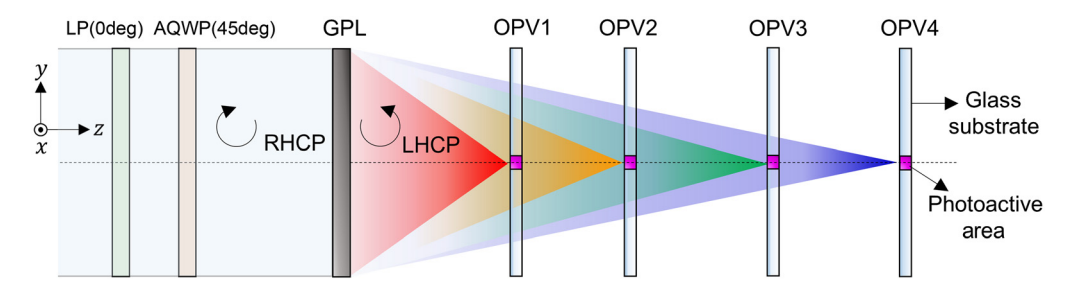


Fig. 4 The CiMOS structure.

Table 1 Optimal focal lengths versus wavelength at different detection planes.

Detector	OPV1	OPV2	OPV3	OPV4
Absorbed center wavelength (nm)	650	550	500	450
Location away from the GPL f (mm)	42.3	50	55	61.1

The GPL produces a spectrally dependent focal length. In this model, we assume that the GPL has a diameter D=25 mm and is designed at a center wavelength $\lambda_0=550$ nm with a design focal length $f_0=50$ mm. Following paraxial ray-tracing analysis, the spectrally dependent focal length is calculated as

$$f(\lambda) = \frac{\lambda_0}{\lambda} f_0. \tag{5}$$

It is worth noting that, from Eq. (5), the GPL focuses longer wavelengths at shorter focal lengths. This is unlike refractive lenses that focus shorter wavelengths at shorter focal lengths.

The CiMOS device is designed here to absorb four spectrally narrowband signals at wavelengths 650, 550, 500, and 450 nm. Thus, we place four OPV detectors at the focal lengths given in Table 1. The OPV's shape and photoactive area determine how narrow the detected spectral bands are, with smaller and larger OPV's active areas yielding narrower and broader spectral bands, respectively.

We modeled the light-gathering coefficient $\kappa(f,\lambda)$ of each OPV as a function of wavelength and focal length. We defined this coefficient as the ratio of the optical power that is contained (focused) within the OPV's active area to the total optical power (for a given focal length and wavelength). To this end, we first determined the shape and width of the PSF, which is the system's impulse response to a point source. Using the ray-tracing model, the geometrical equivalence of the PSF width is calculated as

$$w(f,\lambda) \cong \begin{cases} 2.44\lambda \frac{f}{D} & \text{if } \lambda = \lambda_0 \\ D\left(\frac{\lambda}{\lambda_0} - 1\right) & \text{otherwise} \end{cases}$$
 (6)

where the first condition refers to the diffraction-limited spot size. If we assume that the GPL is contained within a circular aperture, the PSF is expressed as

$$PSF(f,\lambda) \approx \left[\frac{2J_1(2.44\pi\rho/w)}{2.44\pi\rho/w} \right]^2, \tag{7}$$

where $J_1(x)$ denotes the Bessel function of the first-order of the first kind and $\rho = \sqrt{(x')^2 + (y')^2}$ is the radial distance from the center of the detection plane, represented by the Cartesian coordinates x' and y'. The PSFs at the various detection planes and wavelengths given in Table 1 were simulated in the spatial range from -0.05 to +0.05 mm for the diffraction-limited condition and from -5 to +5 mm for all other wavelengths. Figures 5 and 6 show the simulated 2D plots of the incoherent and coherent PSFs at various detection planes and wavelengths, respectively. It is worth noting that only the portion of the PSF that is contained within the OPV's area contributes to the photocurrent generation. All defocused light outside the OPV's active region is either lost in the case of a single-pixel CiMOS or contributes to a spectral crosstalk term in the case of 2D FP CiMOS.

The light-gathering coefficient is then given as

$$\kappa(f,\lambda) = \eta_{+1}(\lambda) \frac{\int_{-a}^{a} \int_{-b}^{b} PSF(f,\lambda) dx' dy'}{\int_{-\infty}^{\infty} \int_{-\infty}^{\infty} PSF(f,\lambda) dx' dy'},$$
(8)

where a and b are the distances from the center of the OPV's active region to its boundary.

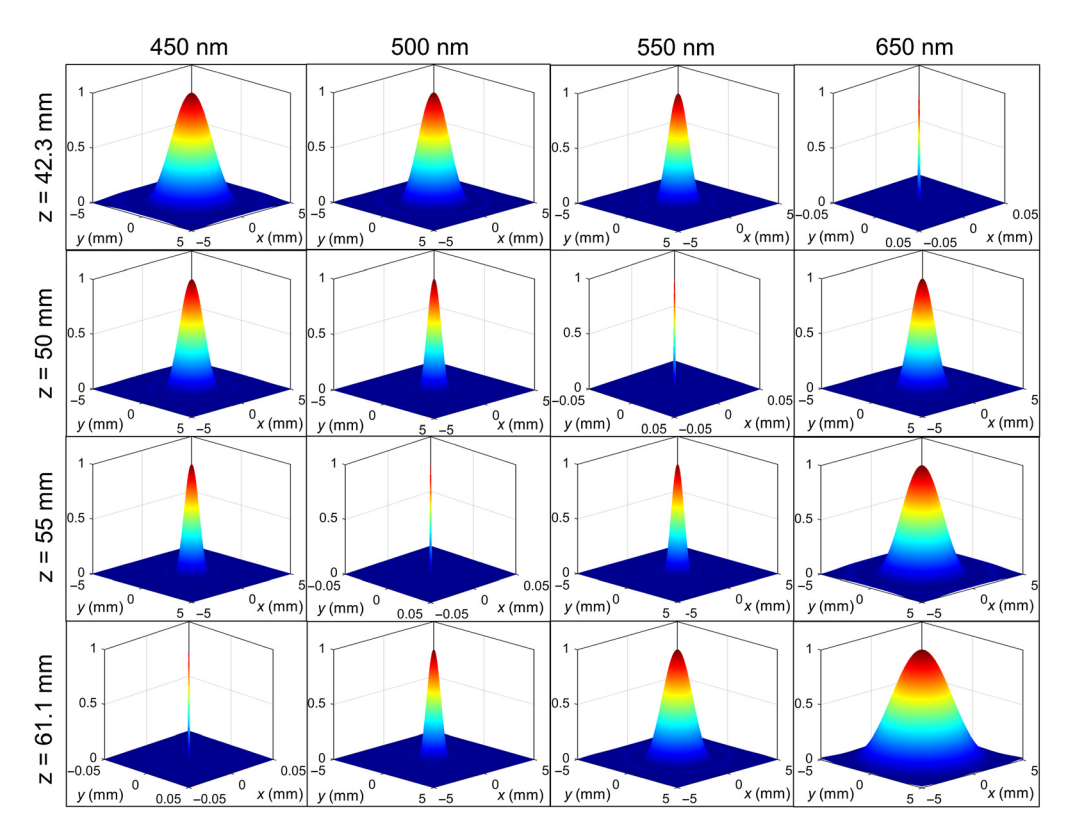


Fig. 5 Plots of the 2D PSF at detection planes z = 42.3, 50, 55, and 61 mm and wavelengths $\lambda = 450$, 500, 550, and 650 nm.

In our model, we assumed that the OPV's active area is a square of dimensions 0.5 mm \times 0.5 mm; therefore, we chose a=b=0.25 mm to compute $\kappa(f,\lambda)$. Additionally, the diffraction efficiency $\eta_{+1}(\lambda)$ was chosen with a profile similar to Fig. 3. The simulated lightgathering coefficient at each detection plane is provided in Fig. 7 sampled from 400 to 800 nm in 1-nm increments.

The simulation results depict four narrowband spectra, centered at the design wavelengths given in Table 1, with maxima that coincide with the diffraction efficiency of the center wavelength. The full width at half maximum (FWHM) spectral bandwidth was calculated to be 67.8, 56, 52.4, and 47 nm for 650-, 550-, 500-, and 450-nm wavelengths, respectively. As mentioned previously, the FP aperture's or detector's pitch (whichever is smaller) determines the spectral resolution of each spectral band. Again, assuming a square detector, we simulated the light-gathering coefficient and its corresponding FWHM at the detection plane (z = 50 mm) using detector pitch values of 0.25, 0.5, 1, and 2 mm, as shown in Figs. 8(a) and 8(b), respectively. As the detector's pitch decreases, the FWHM also decreases. For the 0.25-mm detector's pitch, the FWHM was calculated to be 28 nm, which is half of the FWHM corresponding to the 0.5-mm detector's pitch. Also note that, when the detector's pitch increases, both the FWHM and spectral crosstalk increase, resulting in lower overall contrast.

The results in Fig. 7 do not consider the OPV's transmittance and reflectance losses as well as the OPV's spectral responsivity. To simulate a more practical case, we modeled the generated photocurrent of each OPV shown in Fig. 4. The photocurrent of the *N*'th OPV is calculated as

$$i_N(f,\lambda) = [\gamma(\lambda)]^{N-1} \kappa(f,\lambda) \Re(\lambda) P(\lambda),$$
 (9)

where $\gamma(\lambda)$ is the OPV's transmittance, $\Re(\lambda)$ is the OPV's responsivity, and $P(\lambda)$ is the incident optical power. We assumed all OPVs to be made from the same material with modeled responsivity given in Fig. 9(a). Additionally, the incident optical power is set to 1 μ W/nm, and the OPV's transmittance is $\gamma = 0.9$ flat across the entire spectrum. The simulated OPV's photocurrent is provided in Fig. 9(b). To further improve the OPV's photocurrent, one can either

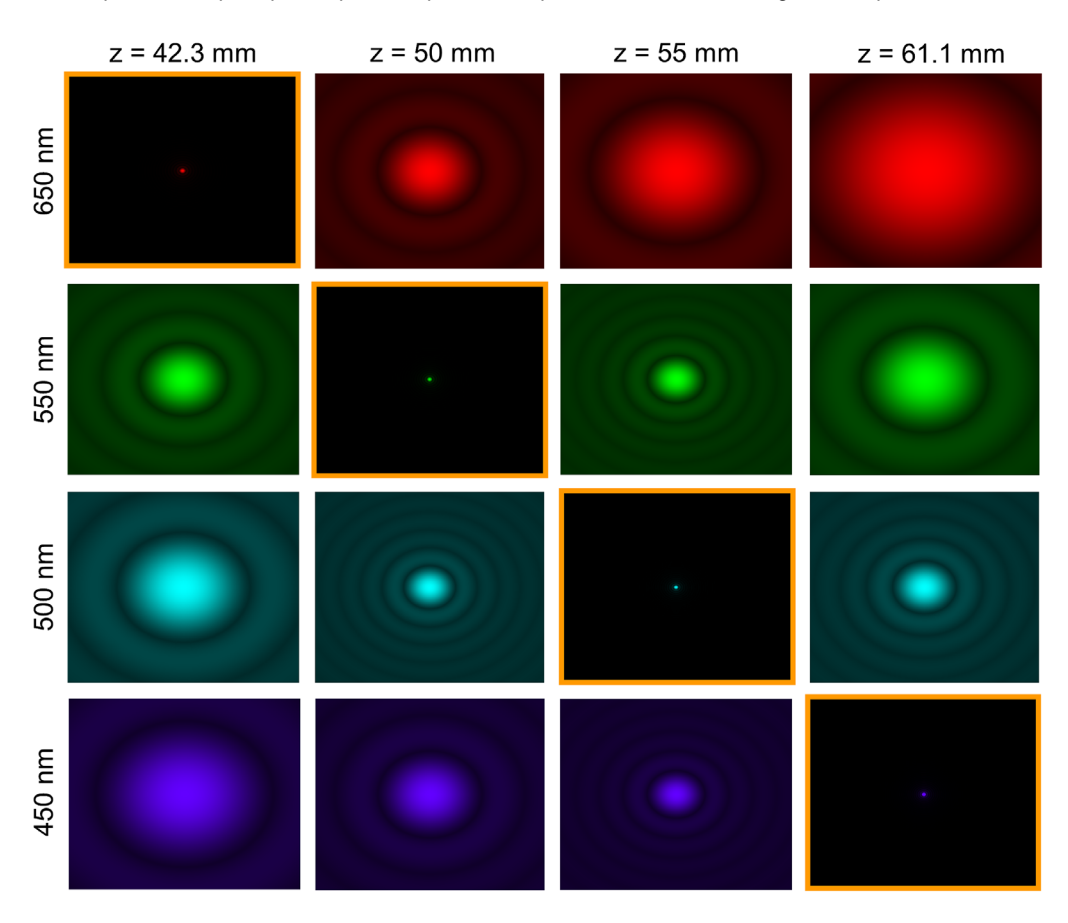


Fig. 6 A top-view plot of the PSFs at detection planes z = 42.3, 50, 55, and 61 mm and wavelengths $\lambda = 450$, 500, 550, and 650 nm.

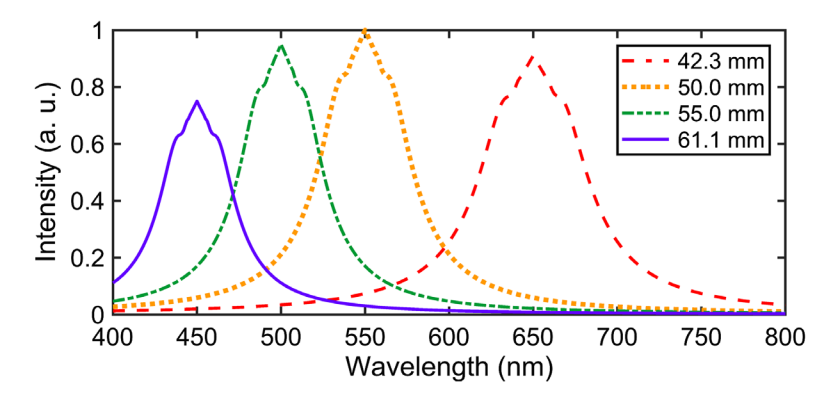


Fig. 7 Simulated light-gathering coefficients at detection planes z = 42.3, 50, 55, and 61 mm.

(i) increase the GPL's diffraction efficiency, (ii) increase the input optical power, (iii) design OPV cells with lower reflective (higher transmissive) electrodes, or (iv) use OPV cells with better spectral responsivity.

5 Experimental Results

A proof of concept of a single-pixel CiMOS device is demonstrated experimentally. All OPVs were fabricated from the same material using a bulk-heterojunction device architecture and responsivities shown in Figs. 10(a) and 10(b), respectively. A highly transparent indium tin oxide (ITO) on a glass substrate was used with transmittance over 90% across the visible (VIS)

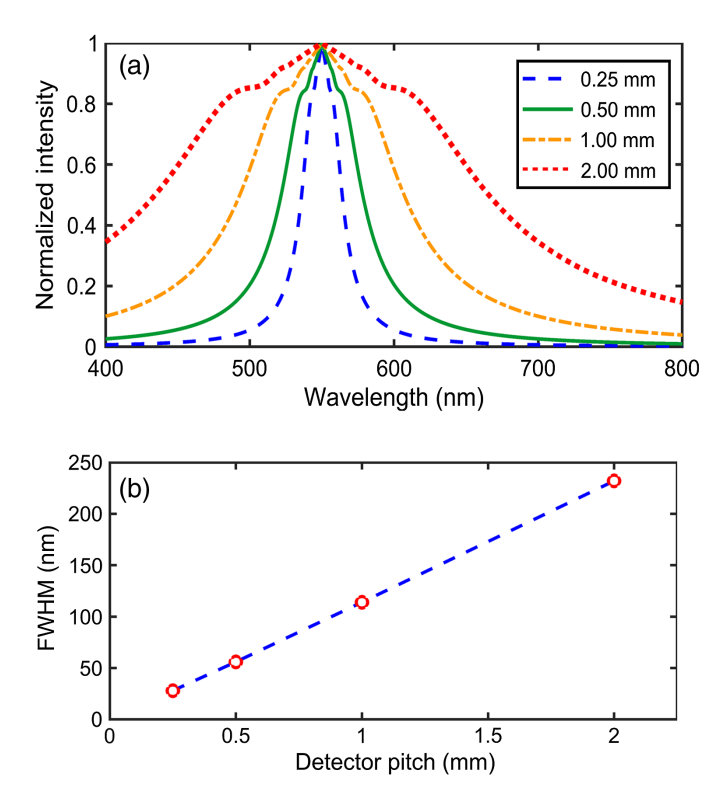


Fig. 8 (a) The spectral response of the 50-mm detection plane for detector pitch of 0.25 mm (dashed line), 0.5 mm (solid line), 1 mm (dotted-dash line), and 2 mm (dotted line) and (b) the FWHM spectral bandwidth versus the detector pitch.

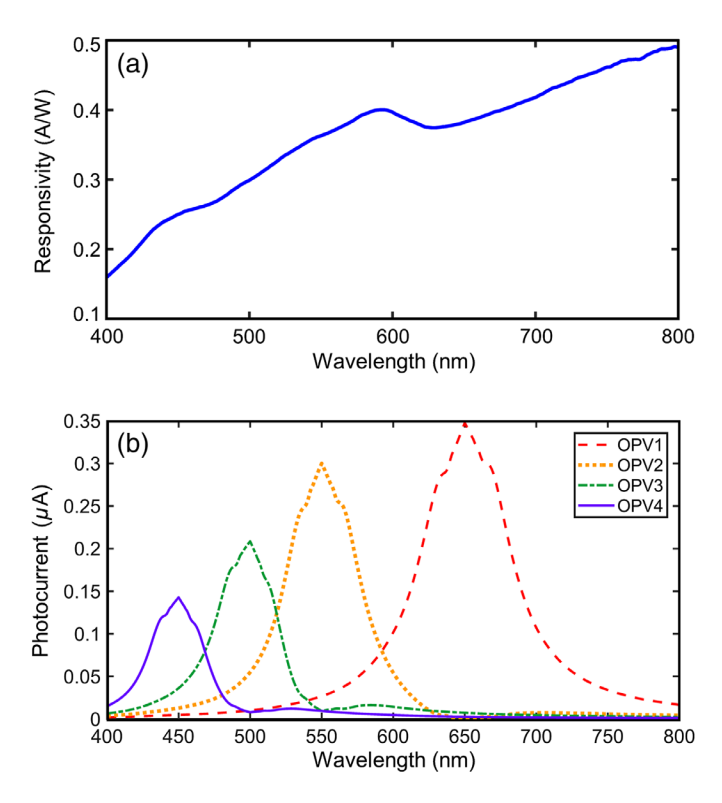


Fig. 9 (a) Modeled OPV responsivity and (b) simulated OPV spectral response.

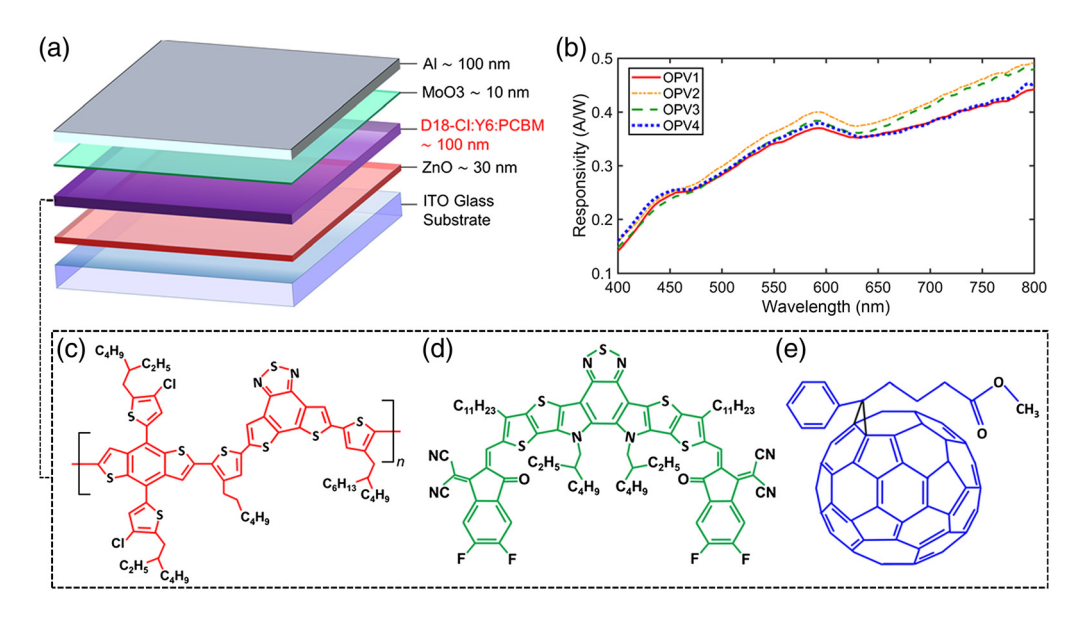


Fig. 10 (a) OPV device architecture; (b) measured OPV responsivities and chemical structures of (c) D18-Cl; (d) Y6 BTP-4F; and (e) PCBM.

spectrum. A 30-nm zinc oxide (ZnO) was deposited on top of the substrate serving as the electron transport layer followed by the active layer having a 100-nm thickness. The active layer consisted of a ternary blend of copolymer donor D18-Cl, a non-fullerene small molecule acceptor Y6 (BTP-4F), and a fullerene-based small molecule acceptor PCBM with a blend ratio of 1:1.6:0.2, respectively, processed with a concentration of 14 mg/ml in chloroform. The chemical structures of these molecules are provided in Figs. 10(c)-10(e). A thin layer (10 nm) of molybdenum trioxide (MoO₃) hole transport layer was then deposited on top of the active layer, followed by aluminum (Al) as the anode layer with a thickness of 100 nm. The total OPV device thickness (excluding the substrate) was ~240 nm. Additionally, the photoactive region was a square with a 0.5-mm pitch.

We used a commercial GPL (Edmund Optics #34–464 polarization directed flat lens) with a diameter D=25 mm, a thickness t=0.45 mm, and a design wavelength $f_0=50$ mm at design wavelength $\lambda_0=550$ nm.

The experimental setup is shown in Fig. 11. In this experiment, we measured the spectral response of OPV1-4 from 400 to 800 nm using a monochromator and a broadband xenon arc lamp. The OPVs' photocurrents were measured using a Burr-Brown charge integrator circuit (ACF2101) that supplied a voltage related to the OPVs' photocurrent as

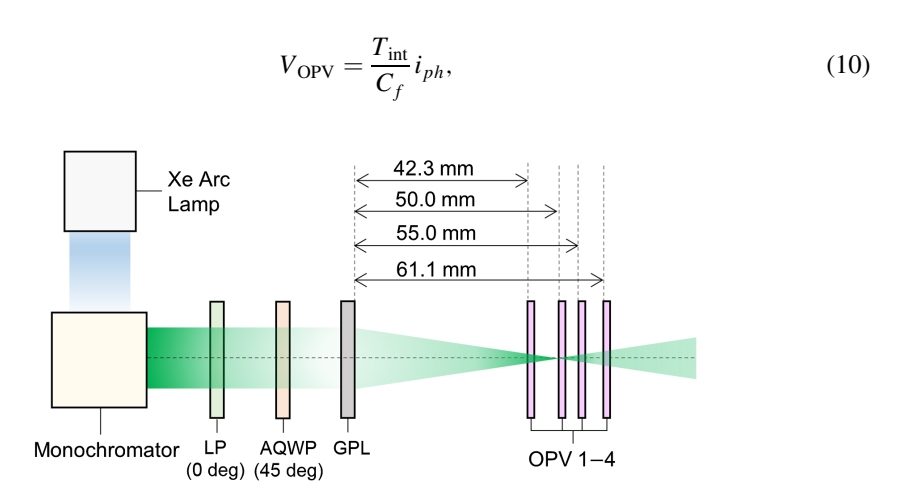


Fig. 11 Experimental setup of the CiMOS structure.

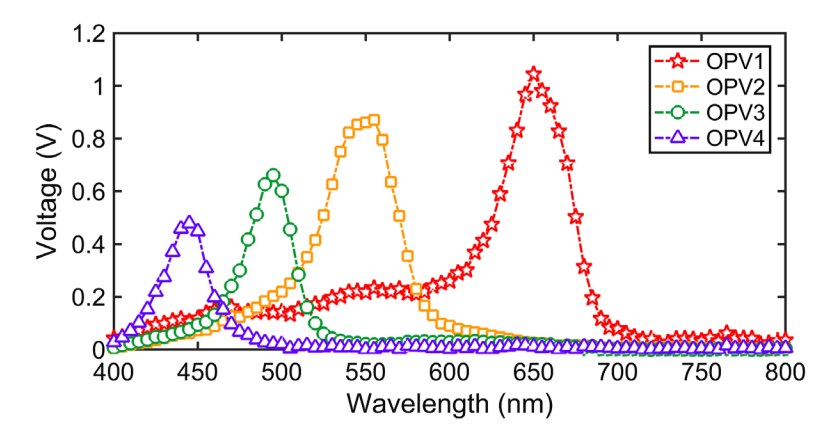


Fig. 12 Measured CiMOS spectral response.

where $T_{\rm int}$ is the circuit's integration time, and C_f is the feedback integration capacitance. These parameters were set to $T_{\rm int}=16.67$ ms and $C_f=1000$ pf. The output of the monochromator was collimated and then travelled on-axis passing through an LP oriented at 0 deg with respect to the x axis, followed by an AQWP with its fast axis oriented at 45 deg with respect to the x axis. To accurately determine the fast axis of the AQWP, it was initially placed between two crossed polarizers and then rotated until a minimum intensity was measured by an integrating spherebased radiometer, indicating that the AQWPs axis is parallel to the LPs axis. The AQWP was then rotated by 45 deg.

Finally, the OPV layers were placed away from the GPL by the focal lengths shown in Fig. 11. This enabled the GPL to (theoretically) focus 650-, 550-, 500-, and 450-nm light at the detection plane of OPV1, 2, 3, and 4, respectively.

The measured spectral response of each OPV is shown in Fig. 12. We observe some similarities and differences between the measurements and the simulated OPV's spectral response in Fig. 9. Alhough the general pattern of a tapering amplitude and FWHM (from OPV1 to OPV4) are similar to the simulation results, there are some notable differences, including a shift of the OPV3's and OPV4's center wavelengths by ~5 nm and larger spectral crosstalk exhibited by OPV1 for wavelengths below 610 nm. The center wavelength shift for OPV3 and OPV4 could likely be due to the slight displacement of these detectors away from their optimal focal lengths. Additionally, the higher spectral crosstalk of OPV1 could be caused by a different detector geometry (width and height of the active region) allowing more light to be absorbed for out-of-band wavelengths.

We also quantified the root-mean-square deviation (RMSD) between the measured and simulated results. This was achieved by normalizing both the measured and simulated results to the corresponding maximum value of OPV1 response. The calculated RMSD values between the experimental and theoretical values are provided in Table 2. As expected, OPV1 displays the largest error due to the large spectral leakage whereas OPV2-4 has comparable RMSD values. Furthermore, we numerically quantified the out-of-band spectral leakage for each OPV. We first defined the in-band spectral range as the region encompassing each OPV's center wavelength ± 50 nm. For example, the in-band spectral range for OPV1 (center wavelength of 650 nm) spans 600 to 700 nm. Therefore, the out-of-band spectra were defined as the regions lying outside the in-band range and the within 400- to 800-nm bandwidth. Based on these assumptions, we calculated the spectral leakage by taking the ratio of the area under the curve for the out-of-band wavelengths to that of the entire spectrum from 400 to 800 nm. We applied this calculation to

Table 2 RMSD between the measured spectral response and simulated response for each OPV cell.

Detector	OPV1	OPV2	OPV3	OPV4
RMSD	0.112	0.051	0.054	0.040

Table 3 Out-of-band spectral leakage (%) for the simulated and measured OPV detector response.

Detector	OPV1	OPV2	OPV3	OPV4
Simulation	26.2%	16.7%	18.2%	14.8%
Experiment	40%	20.4%	17.4%	12.5%

both the simulated and measured spectra in Figs. 9(b) and 12, respectively. The results of the outof-band spectral leakage are provided in Table 3. We note that the theoretical and experimental leakage results are comparable for OPV2-4 with absolute difference in the spectral leakage of <4% (3.7%, 0.8%, and 2.3% for OPV 2, 3, and 4, respectively). However, the measured OPV1 spectral response exhibited notably larger leakage relative to the simulated response with an absolute difference of 13.8%. This large spectral leakage in OPV1 could likely be caused by a geometrical mismatch between the fabricated cell and the theoretical model of OPV1's photoactive area. Additionally, any optical misalignment or tilt in the GPL or OPV detectors could cause the OPV cell to preferentially absorb specific colors more than others (i.e., be biased toward the blue or red wavelengths depending on the tilt direction). To validate this, we considered an OPV cell with a size tolerance of $\pm 10\%$ of the modeled OPV size (0.5 mm \times 0.5 mm) and an xy displacement tolerance of $\pm 10\%$. This causes the simulated leakage to rise by 14.7% (at the maximum tolerance limit of +10%) yielding an overall leakage of 40.9%, which is similar to the experimental leakage of OPV1. Overall, while the out-of-band spectral leakages are not fully suppressed (especially toward shorter wavelengths as in the OPV1 response), this issue can be resolved by fine tuning the OPVs' geometrical structure (width and height of the photoactive area) and optical alignment. The latter requires all of the optics (GPL and OPVs) to be aligned along the same optical axis and the detectors to not be tilted about the xy plane. Additionally, decreasing the detector's pitch can also minimize the out-of-band spectral response, as can be observed from Fig. 8(a).

Although we experimentally demonstrated a single-pixel CiMOS structure for four-color sensing, future directions involve upgrading the CiMOS to a 2D image sensor. This will require using GPMLA for imaging on a focal volumetric array composed of multiple stacked organic semiconductors FP arrays. The use of GPLMA for imaging has been demonstrated previously in the snapshot channeled imaging spectrometer sensor.³⁴ Moreover, prior demonstrations of organic image sensors using complementary metal-oxide semiconductors have showcased high-performance imaging capabilities.^{42,43} Some important considerations for the 2D CiMOS design include performing spectral crosstalk analysis between adjacent OPVs (pixels) and modeling the system's modulation transfer function to evaluate the spatial resolution and contrast performance of the 2D CiMOS structure.

Moreover, the CiMOS proof of concept was limited to the detection of 4 spectral bands in the VIS range. This concept can be further extended to the near-infrared (NIR) spectra when using a VIS/NIR-sensitive GPL, which has been previously demonstrated.⁴⁴ Leveraging both the VIS and NIR spectra, the CiMOS sensor can offer utilities in remote sensing and agriculture applications, e.g., quantifying vegetation health based on the photochemical reflectance index^{45,46} or based on the normalized difference vegetation index.⁴⁷

If designed and implemented correctly, the CiMOS structure showcases many advantages not found in other MSI architectures, including its simplicity (in that only GPMLA and OPVs made from the same material are required), compactness, ability to achieve aberration-free performance, and high diffraction efficiency as compared with conventional diffractive lenses and gratings. These advantages may make it attractive to a wide range of applications spanning agriculture to medicine.

6 Conclusion

Multispectral sensing is an attractive method that is often used for detecting the chemical features of objects. In this paper, we have presented a novel multispectral sensor inspired by the

cephalopod's eyes. The sensor leverages the strong longitudinal CA present in geometric phase lenses to focus multiple colors at different focal planes. Each plane contains a semitransparent OPV that absorbs the focused light and transmits the defocused light. Simulations have been conducted to quantify the sensor spectral resolution and efficiency versus different lens and detector parameters, including the GPL's diffraction efficiency and design wavelength and the detector photoactive area. A proof of concept of the new sensor has also been presented showcasing the ability to detect four unique spectra, with FWHM as low as 35 nm. The RMSD values between the theory and experimental results have also been provided with error spanning 0.04 to 0.11 with an average value of 0.06. Error sources have been attributed to the detectors' slight displacement away from their optimal focal length and to the imperfect geometrical design of the detectors' active area. Further reduction in the RMSD error can be achieved with better optical alignment and more precise detector geometrical design. The new sensor is marked by its simple, compact structure with the potential ability to achieve aberration-free performance and nearunity diffraction efficiency. This sensor will be beneficial in various applications that require analyzing the chemical nature of targets, such as agriculture, biomedicine, and environmental monitoring.

Acknowledgments

This work was supported by the National Science Foundation (Grant No. 1809753).

References

- 1. R. M. Levenson and J. R. Mansfield, "Multispectral imaging in biology and medicine: slices of life," *Cytometry Part A* **69A**(8), 748–758 (2006).
- F. Vasefi, N. MacKinnon, and D. L. Farkas, "Hyperspectral and multispectral imaging in dermatology," *Imaging Dermatol.* 2016, 187–201 (2016).
- 3. S. C. Kefauver, J. Peñuelas, and S. L. Ustin, "Applications of hyperspectral remote sensing and GIS for assessing forest health and air pollution," in *IEEE Int. Geosci. and Remote Sens. Symp.*, IEEE, pp. 3379–3382 (2012).
- 4. U. R. Balasubramanian, J. Saravanavel, and S. Gunasekaran, "Ore mineral discrimination using hyperspectral remote sensing—a field-based spectral analysis," *Arab. J. Geosci.* **6**(12), 4709–4716 (2013).
- 5. F. J. Crosby, "Stokes vector component versus elementary factor performance in a target detection algorithm," *Proc. SPIE* **5432**, 1–11 (2004).
- 6. K. Homma et al., "Application of an imaging spectropolarimeter to agro-environmental sciences," *Proc. SPIE* **5234**, 638 (2004).
- 7. G. Vane et al., "The airborne visible/infrared imaging spectrometer (AVIRIS)," *Remote Sens. Environ.* **44**(2–3), 127–143 (1993).
- 8. P. Mouroulis, R. O. Green, and T. G. Chrien, "Design of pushbroom imaging spectrometers for optimum recovery of spectroscopic and spatial information," *Appl. Opt.* **39**(13), 2210 (2000).
- 9. J. Brauers, N. Schulte, and T. Aach, "Multispectral filter-wheel cameras: geometric distortion model and compensation algorithms," *IEEE Trans. on Image Process.* **17**(12), 2368–2380 (2008).
- 10. N. Hagen and M. W. Kudenov, "Review of snapshot spectral imaging technologies," *Opt. Eng.* **52**(9), 090901 (2013).
- 11. M. Garcia et al., "Bioinspired polarization imager with high dynamic range," *Optica* **5**(10), 1240 (2018).
- 12. A. Altaqui et al., "Mantis shrimp–inspired organic photodetector for simultaneous hyperspectral and polarimetric imaging," *Sci. Adv.* 7(10), eabe3196 (2021).
- 13. C. Liu et al., "Bio-inspired multimodal 3D endoscope for image-guided and robotic surgery," *Opt. Express* **29**(1), 145 (2021).
- 14. Y. Zhao et al., "Multiband polarization imaging," J. Sens. 2016, 1-10 (2016).

- 15. A. Altaqui et al., "Organic-based photodetectors for multiband spectral imaging," *Appl. Opt.* **60**(8), 2314–2323 (2021).
- 16. A. Altaqui et al., "Bio-inspired spectropolarimetric sensor based on tandem organic photo-detectors and multi-twist liquid crystals," *Opt. Express* **29**(26), 43953–43969 (2021).
- 17. R. Futahashi, "Color vision and color formation in dragonflies," *Curr. Opin. Insect Sci.* **17**, 32–39 (2016).
- 18. Y. Wang et al., "Chameleon-inspired structural-color actuators," *Matter* **1**(3), 626–638 (2019).
- 19. M.-S. Steiner et al., "Chromogenic sensing of biogenic amines using a chameleon probe and the red–green–blue readout of digital camera images," *Anal. Chem.* **82**(20), 8402–8405 (2010).
- 20. L. M. Mäthger et al., "Color blindness and contrast perception in cuttlefish (*Sepia officinalis*) determined by a visual sensorimotor assay," *Vis. Res.* **46**(11), 1746–1753 (2006).
- A. L. Stubbs and C. W. Stubbs, "Spectral discrimination in color blind animals via chromatic aberration and pupil shape," *Proc. Natl. Acad. Sci. U. S. A.* 113(29), 8206–8211 (2016).
- 22. S. Zhan et al., "Hyperspectral imaging bioinspired by chromatic blur vision in color blind animals," *Photonics* **6**(3), 91 (2019).
- 23. S. Zhan et al., "Spectral discrimination and spatial resolution from retinal chromatic blur images in color blind animals," *Spectrosc. Lett.* **53**(5), 349–359 (2020).
- 24. M. J. Escuti, J. Kim, and M. W. Kudenov, "Controlling light with geometric-phase holograms," *Opt. Photonics News* **27**(2), 22–29 (2016).
- 25. J. Kim et al., "Fabrication of ideal geometric-phase holograms with arbitrary wavefronts," *Optica* **2**(11), 958–964 (2015).
- Y.-H. Lee et al., "Recent progress in Pancharatnam–Berry phase optical elements and the applications for virtual/augmented realities," *Opt. Data Process. Storage* 3(1), 79–88 (2017).
- 27. S. Moon et al., "Augmented reality near-eye display using Pancharatnam–Berry phase lenses," *Sci. Rep.* **9**(1), 6616 (2019).
- 28. P. Sen et al., "Panchromatic all-polymer photodetector with tunable polarization sensitivity," *Adv. Opt. Mater.* 7(4), 1801346 (2018).
- 29. G. Pace et al., "All-organic and fully-printed semitransparent photodetectors based on narrow bandgap conjugated molecules," *Adv. Mater.* **26**(39), 6773–6777 (2014).
- 30. M.-B. Lien et al., "Ranging and light field imaging with transparent photodetectors," *Nat. Photonics* **14**(3), 143–148 (2020).
- 31. M. Khorasaninejad et al., "Multispectral chiral imaging with a metalens," *Nano Lett.* **16**(7), 4595–4600 (2016).
- 32. O. Avayu et al., "Composite functional metasurfaces for multispectral achromatic optics," *Nat. Commun.* **8**(1), 14992 (2017).
- 33. X. Zou et al., "Imaging based on metalenses," *PhotoniX* 1(1), 2 (2020).
- 34. Y. Wang, M. J. Escuti, and M. W. Kudenov, "Snapshot channeled imaging spectrometer using geometric phase holograms," *Opt. Express* **27**(11), 15444–15455 (2019).
- 35. FireFly5, "Closeup of Cuttlefish Eye Showing W-Shaped Pupil," Wikimedia Commons, https://commons.wikimedia.org/wiki/File:Cuttlefish_eye.jpg (2014).
- 36. L. M. Mäthger et al., "The W-shaped pupil in cuttlefish (Sepia officinalis): functions for improving horizontal vision," *Vis. Res.* **83**, 19–24 (2013).
- 37. J. G. Sivak, "Shape and focal properties of the cephalopod ocular lens," *Can. J. Zool.* **69**(10), 2501–2506 (1991).
- 38. C. M. Talbot and J. N. Marshall, "The retinal topography of three species of coleoid cephalopod: significance for perception of polarized light," *Philos. Trans. R. Soc. B: Biol. Sci.* **366**(1565), 724–733 (2011).
- 39. C. Yousefzadeh et al., "'Achromatic limits' of Pancharatnam phase lenses," *Appl. Opt.* **57**(5), 1151–1158 (2018).
- 40. K. J. Hornburg et al., "Design and fabrication of an aspheric geometric-phase lens doublet," *Proc. SPIE* **10735**, 1073513 (2018).

- 41. J. Kim et al., "Chromatic-aberration correction in geometric-phase lenses, for red, green, and blue operation (conference presentation)," *Proc. SPIE* **10361**, 1036113 (2017).
- 42. S.-J. Lim et al., "Organic-on-silicon complementary metal—oxide—semiconductor colour image sensors," *Sci. Rep.* **5**(1), 7708 (2015).
- 43. M. G. Han et al., "Narrow-band organic photodiodes for high-resolution imaging," *ACS Appl. Mater. Interfaces* **8**(39), 26143–26151 (2016).
- 44. B. Piccirillo et al., "Flat polarization-controlled cylindrical lens based on the Pancharatnam–Berry geometric phase," *Eur. J. Phys.* **38**(3), 034007 (2017).
- 45. J. A. Gamon, J. Peñuelas, and C. B. Field, "A narrow-waveband spectral index that tracks diurnal changes in photosynthetic efficiency," *Remote Sens. Environ.* **41**(1), 35–44 (1992).
- 46. G. G. Drolet et al., "A MODIS-derived photochemical reflectance index to detect interannual variations in the photosynthetic light-use efficiency of a boreal deciduous forest," *Remote Sens. Environ.* 98(2), 212–224 (2005).
- 47. A. B. Potgieter et al., "Multi-spectral imaging from an unmanned aerial vehicle enables the assessment of seasonal leaf area dynamics of sorghum breeding lines," *Front. Plant Sci.* **8**, 1532 (2017).

Ali Altaqui received his BE (Hons) and MPhil degrees in electrical engineering from the University of Sydney in Australia in 2012 and 2014, respectively. He received his MSc degree and PhD in electrical engineering, from North Carolina State University. During his PhD, he worked in the Optical Sensing Lab under the direction of Dr. Michael Kudenov. His research focused on developing new optical sensor architectures based on organic photodetectors for polarization and hyperspectral imaging. Applications include remote sensing, biomedical imaging, food safety, agriculture, and astronomy.

Harry Schrickx received his BS degree in mechanical engineering from North Carolina State University in 2018. He is currently a PhD student in mechanical engineering at North Carolina State University under the direction of Dr. Brendan O'Connor. His research focuses on fabricating and characterizing aligned semiconducting polymer films for polarization-sensitive photodetectors.

Sydney Gyurek is a student at North Caroline State University majoring in electrical and computer engineering with a minor in Chinese studies. She currently does undergraduate research under Dr. Kudenov and assisted Dr. Altaqui in data collection.

Pratik Sen received his BS (Hons) degrees and PhD in mechanical engineering from North Carolina State University in 2014 and 2019, respectively. His doctoral work was under the supervision of Dr. Brendan O'Connor; his research focused on fabricating and characterizing organic photovoltaics and photodetectors for novel optical sensing technologies.

Michael Escuti received his MSc degree and PhD from Brown University in 1999 and 2002, respectively, and his BSc degree from Drexel University in 1997, all in electrical engineering. He served as a postdoctoral fellow at Eindhoven University of Technology (Netherlands), in the Department of Chemistry and Chemical Engineering. As of late 2019, he has been named an inventor on 19/23 US patents/applications, published 60 peer-reviewed journal publications, published 85 conference proceedings, delivered 34 invited research talks, and co-authored two invited magazine articles and one book chapter. He has been recognized by the 2016 NCSU Innovator of the Year Award, the 2010 Presidential Early Career Award for Scientists and Engineers (National Science Foundation), and both the Glenn H. Brown Award (2004) from the International Liquid Crystal Society (ILCS) and the OSA/NewFocus Student Award (2002) from the Optical Society of America (OSA) for his PhD research.

Brendan T. O'Connor is a professor of mechanical and aerospace engineering at North Carolina State University in Raleigh, North Carolina. He received his BS degree from Marquette University in 2000, his MS degree from the University of Massachusetts, Amherst in 2004, and his PhD from the University of Michigan, Ann Arbor in 2009, all in mechanical engineering. After receiving his PhD, he was an NRC-NIST postdoctoral fellow at the National

Institute of Standards and Technology (NIST). He became a faculty member at NC State in 2011. His research interests include organic electronic process-structure-property relationships, opto-electronic devices, and polymer mechanics.

Michael Kudenov is an associate professor of electrical and computer engineering at North Carolina State University in Raleigh, North Carolina. He received his BS degree from the University of Alaska Fairbanks in 2005 in electrical engineering and his PhD from the University of Arizona in 2009 in optical sciences. His research focuses on the development, calibration, and validation of new spectral and polarimetric imaging systems for wavelengths spanning the UV to the thermal IR, including high speed and snapshot imaging spectrometers, polarimeters, cross-correlation spectrometers, and spectropolarimeters. Applications include space situational awareness, chemical imaging, quality control, optical modeling and calibration, agriculture, and phenotyping.